

Parameter Space Comparison of Inertial Particle Models

Jérôme Holbein and Tobias Günther

Computer Graphics Laboratory, ETH Zürich, Switzerland

Abstract

In many meteorological and engineering problems, the motion of finite-sized objects of non-zero mass plays a crucial role, such as in air pollution, desertification, stirring of dust during helicopter navigation, or droplets in clouds or hurricanes. The motion of these so-called inertial particles can be modeled by equations of motion that place certain application-specific assumptions. These models are determined by parameters, such as the particle size, the Stokes number or the density ratio between particle and fluid. To describe the motion of finite-sized particles in an accurate and feasible way, one has to choose the most suitable particle model and its model parameters very carefully. In this paper, we present multiple interactive visualizations that allow us to compare different inertial particle models for a range of model parameters. To assess the similarities and disparities in the inertial pathline geometries in space-time, we first trace multiple inertial particles with varying model parameters from the same seed point and visualize their motion in space-time for different inertial particle models. Further, we find for a given inertial trajectory in one model, the parameters of the other model that fit this trajectory best. Finally, we offer a quantitative view of the pair-wise inertial trajectory distance for each possible parameter combination of two inertial particle models for a given seed point. By visually exploring this parameter space, we can find similarities and dissimilarities between parameter configurations, which guides the selection of the parameter model. Since all these visualizations only consider one single seed point, we extend the methods by displaying the results for multiple seed points in the same domain or by using stacked visualizations. We apply our method to multiple analytic and numerical vector fields for two inertial particle models.

This is the authors preprint. The definitive version is available at <http://diglib.ethz.ch/>.

1. Introduction

The scientific visualization of inertial particles is concerned with the motion of finite-sized objects of non-zero mass in fluid flows [GT17]. Traditionally, flow visualization uses massless tracer particles, since they follow the flow perfectly tangential. While this has a long tradition, cf. McLoughlin et al. [MLP*10], it is of limited use when scientists are interested in the impact of the particle mass on the motion of inertial particles. The considerable influence of mass, compared to massless particles can for instance be observed in meteorological simulations [SRCV98, SH09], sand saltation modeling [SL99], visual obscuration in helicopter landings [SGL10, KGRK14], jellyfish feeding [PD09] and the tracking of toxic elements [NWE74]. The motion of these finite-sized inertial particles can be modeled by ordinary differential equations under certain simplifying conditions. Each model depends on one or more parameters. The choice of the most suitable model is a difficult task, as the difference between the models varies spatially. How can we compare these models and their parameter spaces? Are there parameter choices where the inertial pathlines are nearly identical? Which parameter in a one-parametric model can approximate a trajectory formed by the two-parametric model best and vice versa? To answer these questions, we propose an

interactive visualization tool that allows us to compare two different inertial particle models under varying model parameters.

Our method provides three coordinated views. First, a qualitative view visualizes inertial trajectories for a possible parameter range in space-time, which yields a surface in case of a one-parameter model and a volume in case of a two-parameter model. Displaying the trajectories for these two models simultaneously allows for a first comparison of space-time overlaps, similarities and disparities between the trajectories of different models. Second, we search for a parameter configuration of one model that leads to the most similar trajectory of the second model. Third, we provide a quantitative approach that explores for a given seed point the space of all possible model parameters. For a one-parametric and a two-parametric model, the parameter space adds up to a 3D space, in which every point uniquely identifies a trajectory for each model. For each point in this space, we compute the distance between the two trajectories, and visualize the resulting scalar field for the full parameter space, which displays the full range of all possible parameter combinations. By displaying this parameter space for multiple seed points in a stacked visualization, we obtain a spatial view on salient regions of similar or dissimilar particle behavior.

2. Related Work

2.1. Inertial Particle Models

We consider two different inertial particle models that are frequently used in the CFD literature. Both models were derived from the Maxey-Riley equations [MR83, FH15], which describe inertial particle motion for small spherical objects. Inertial particles are transported by a vector field $\mathbf{u}(\mathbf{x}, t) : D \times T \mapsto \mathbb{R}^2$ for $D \subseteq \mathbb{R}^2$, $T \subseteq \mathbb{R}$. Further, let $\frac{D\mathbf{u}}{Dt}$ be the material derivative.

One-parametric Model (Model 1). Crowe et al. [CST98] described an inertial particle model, which can be rephrased as an autonomous ODE in phase space, cf. [GT14, GT15]:

$$\frac{d}{dt} \begin{pmatrix} \mathbf{x} \\ \mathbf{v} \\ t \end{pmatrix} = \begin{pmatrix} \mathbf{v} \\ \frac{\mathbf{u}(\mathbf{x}, t) - \mathbf{v}}{r} + \mathbf{g} \\ 1 \end{pmatrix}, \quad \begin{pmatrix} \mathbf{x} \\ \mathbf{v} \\ t \end{pmatrix} (0) = \begin{pmatrix} \mathbf{x}_0 \\ \mathbf{v}_0 \\ t_0 \end{pmatrix} \quad (1)$$

with the initial position \mathbf{x}_0 , initial velocity \mathbf{v}_0 and seed time t_0 , a gravity vector \mathbf{g} and the particle response time r :

$$r = \frac{d_p^2 \rho_p}{18\mu} \quad (2)$$

which consists of particle diameter d_p , particle density ρ_p and air viscosity μ . This model assumes that particles are rigid spheres and that the density of the surrounding air is far smaller than the particle density $\rho_f \ll \rho_p$, which allows us to neglect buoyancy. Further, particle-particle collisions are ignored and one-way coupling is assumed, i.e., particles have no influence on the air flow. These assumptions are common and have been made in numerous applications, cf. [BBC*09, CGP*10, SGL10, BBC*11, KGRK14].

Two-parametric Model (Model 2). The second model allows for higher fluid densities by introducing the density ratio R :

$$R = \frac{2\rho_f}{\rho_f + 2\rho_p} \quad (3)$$

which accounts for buoyancy effects by differentiating aerosols $0 < R < \frac{2}{3}$, bubbles $\frac{2}{3} < R < 2$ and neutrally buoyant particles with $R = \frac{2}{3}$, cf. [HS08]. The motion can be described by, cf. [GT17]:

$$\frac{d}{dt} \begin{pmatrix} \mathbf{x} \\ \mathbf{v} \\ t \end{pmatrix} = \begin{pmatrix} \mathbf{v} \\ \frac{R}{St} (\mathbf{u}(\mathbf{x}, t) - \mathbf{v}) + \frac{3R}{2} \frac{D\mathbf{u}(\mathbf{x}, t)}{Dt} + \left(1 - \frac{3R}{2}\right) \mathbf{g} \\ 1 \end{pmatrix} \quad (4)$$

where St is the Stokes number. Except for the air density being much smaller than the particle density, this model places the same assumptions as the first model above. The second model has found numerous applications [BTT02, BCPP00, VdMG06, HS08, SBR15].

Note that both models approach massless tracer particles in the limit for $r \rightarrow 0$ or $St \rightarrow 0$, respectively.

2.2. Inertial Particles in Visualization

In traditional flow visualization, particles are assumed to be massless, as they are required to follow the flow perfectly tangential, cf. McLoughlin et al. [MLP*10]. Several flow visualization concepts can be extended to inertial particles, though it is important to note that the particle motion itself can vary considerably, cf.

Haller and Sapsis [HS08]. Even though inertial particles have been studied in engineering and physics for decades, their visualization received attention only recently. Early visualizations of inertial particles were created by Roettger et al. [RSBE01], who studied and visualized automotive soiling simulations via heat maps. Günther et al. [GKKT13] extended the concept of integral curves, which led to the introduction of inertial pathlines and new integral curves called *masslines*. A massline connects all particles that were released from the same seed point but with varying mass. Günther et al. extended several other common concepts, such as vortex cores [GT14], finite-time separation [GT15] and vector field topology [GG17]. Recently, Baeza Rojo et al. [BRGG18] visualized the phase space of inertial particles for varying initial conditions. In traditional time-dependent vector fields, Lagrangian coherent structures are often examined, since they constitute material lines that order the flow. Sapsis, Peng and Haller [SH09, PD09, SPH11] calculated hyperbolic Lagrangian coherent structures for inertial particle trajectories. Moreover, Garaboa-Paz and Pérez-Muñuzuri [GPPMn15] and Sagristà et al. [SJJ*17] studied inertial particle separation in the full phase space or in its various subspaces. While backwards integration is a frequently used method for massless tracer particles, the same does not apply for inertial particles. As Günther and Theisel showed, backwards integration of inertial particles is numerically challenging and only feasible for short integration durations [GT17].

Günther and Theisel [GT15] varied the model parameter of the one-parametric model in Eq. (1). We extend their approach to the two-parameter model in Eq. (4) and compare the two models. Additionally, we visualize the closest inertial pathline in the other model and explore the parameter space using stacked visualizations.

2.3. Trajectory Ensemble Visualization

The comparison of inertial trajectories can be seen as ensemble visualization, in which the ensemble parameters change continuously (response time, Stokes number and density ratio). Ferstl et al. [FBW16], Mirzargar et al. [MWK14] and Hummel et al. [HOGJ13] contributed different methods to capture and visualize trajectory variations.

3. Visual Comparison of Particle Models

We propose multiple visualizations to analyze and compare the parameter-dependent motion of the two inertial particle models. With this, we can find conditions in which the models agree, or conversely in which one or both fail. First, we offer in Section 3.1 a space-time visualization of particle trajectories that are determined by certain parameter ranges. This provides a qualitative overview of how varying inertial parameters affect particle motion in both models. In Section 3.2, we examine how close a given trajectory of one model can match any trajectory formed by the other model. We visualize this closest match both for one seed point, as well as for multiple seed points. Finally in Section 3.3, we illustrate the whole parameter space by introducing and plotting different trajectory measures for a range of inertial parameters in both models.

3.1. Space-Time Visualization

To convey the trajectories that can be obtained from varying model parameters, we plot the inertial particle trajectories in space-time.

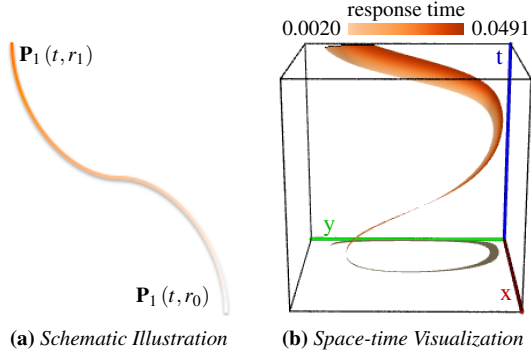


Figure 1: Varying the response time r in Model 1 gives rise to a set of inertial particle trajectories that form a surface. Fig. 1a gives a schematic illustration of the color-coding of r along the front line and Fig. 1b displays the surface for $\tau = 9.95$, $r \in [0.0020, 0.0491]$, and seed $(x_0, y_0, t_0) = (0.5, 0.8, 0)$ in the DOUBLE GYRE flow.

Model 1 Visualization. To describe inertial pathlines of Model 1, we use the concept of an inertial flow map $\phi_{t_0}^\tau(\mathbf{x}_0, \mathbf{v}_0, r)$, which maps an inertial particle with seed point \mathbf{x}_0 , initial velocity \mathbf{v}_0 , seed time t_0 and particle response time r to the location that is reached after integration for duration τ . Using the inertial flow map of Model 1, inertial pathlines $\mathbf{p}_1(\tau, r)$ are defined as in [GKKT13]:

$$\mathbf{p}_1(\tau, r) = \phi_{t_0}^\tau(\mathbf{x}_0, \mathbf{v}_0, r) \quad (5)$$

Continuously varying the model parameter r in a range $[r_0, r_1]$ results in a mass-dependent path surface $\mathbf{P}_1(t, r)$ for $t \in [t_0, t_0 + \tau]$, as used in [GT15]. Throughout the paper, we color-code the response time range from light to dark orange, see Fig. 1 for an example.

Model 2 Visualization. Similarly, the inertial flow map of the second model $\psi_{t_0}^\tau(\mathbf{x}_0, \mathbf{v}_0, R, St)$ depends on two model parameters, density ratio R and Stokes number St . Inertial pathlines are:

$$\mathbf{p}_2(\tau, R, St) = \psi_{t_0}^\tau(\mathbf{x}_0, \mathbf{v}_0, R, St) \quad (6)$$

Since this model has two inertial parameters, all realizations of trajectories form a volume in space-time for ranges of $R \in [R_0, R_1]$ and $St \in [St_0, St_1]$. To display the volume, we visualize the enclosing hull surface, which consists of four mass-dependent path surfaces in which one parameter is fix. The surface spanned by a range of density ratios $R \in [R_0, R_1]$ with a fix Stokes number St_0 is:

$$\mathbf{P}_2^{St_0}(t, R) = \psi_{t_0}^\tau(\mathbf{x}_0, \mathbf{v}_0, R, St_0) \quad (7)$$

for $t \in [t_0, t_0 + \tau]$. The surface spanned by a range of Stokes numbers $St \in [St_0, St_1]$, with a fix density ratio R_0 is:

$$\mathbf{Q}_2^{R_0}(t, St) = \psi_{t_0}^\tau(\mathbf{x}_0, \mathbf{v}_0, R_0, St) \quad (8)$$

The schematic illustration in Fig. 2a illustrates the front lines of the enclosing surfaces, i.e., the four enclosing curves $\mathbf{P}_2^{St_0}(t, R)$, $\mathbf{P}_2^{St_1}(t, R)$, $\mathbf{Q}_2^{R_0}(t, St)$, $\mathbf{Q}_2^{R_1}(t, St)$ at time t . Throughout the paper, we color-code the range of density ratios R in green and the range of Stokes numbers St in blue, see Fig. 2b for an example. Note that these hull surfaces are an approximation, since in space-time inertial particles can intersect and thus in rare cases leave the hull. An exact computation requires progressive sampling of the full volume, which is costly and thus we opt for an approximating solution.

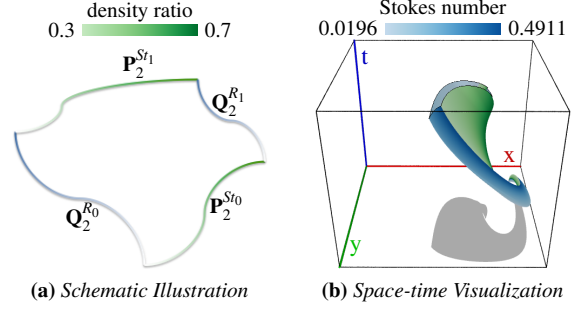


Figure 2: Variation of the two parameters of Model 2 gives rise to a volume in space-time. Fig. 2a shows a schematic illustration of the front lines of the hull surfaces and Fig. 2b shows the surfaces $\mathbf{P}_2^{St_0}$, $\mathbf{P}_2^{St_1}$, $\mathbf{Q}_2^{R_0}$ and $\mathbf{Q}_2^{R_1}$ in space-time, for $\tau = 9.95$, density ratio $R \in [0.3, 0.7]$ and Stokes number $St \in [0.0196, 0.4911]$, with seed point $(x_0, y_0, t_0) = (0.2, 0.8, 0)$ in the DOUBLE GYRE flow.

3.2. Closest Match Visualization

Given a trajectory of one particle model, we are interested in the parameters of the other model that lead to a minimal distance. We call the trajectory with minimal distance the *closest match* to our initial trajectory. This closest match allows us to visualize where the two models can coincide and how large the margin of error is.

Closest Match from Model 1 to Model 2. Given an inertial particle trajectory of Model 1, started at seed point (\mathbf{x}_0, t_0) , with initial velocity \mathbf{v}_0 and response time r_0 . The distance to the closest trajectory of Model 2 is:

$$d_{r_0}^{1 \rightarrow 2}(t) = \min_{\substack{R \in [R_0, R_1] \\ St \in [St_0, St_1]}} \|\phi_{t_0}^{t-t_0}(\mathbf{x}_0, \mathbf{v}_0, r_0) - \psi_{t_0}^{t-t_0}(\mathbf{x}_0, \mathbf{v}_0, R, St)\| \quad (9)$$

Distance $d_{r_0}^{1 \rightarrow 2}$ measures at a certain time t the minimum distance that a point on the Model 1 trajectory has to the points of Model 2 trajectories with model parameters in $[R_0, R_1]$ and $[St_0, St_1]$. The model parameters R^* and St^* that lead to the closest match are:

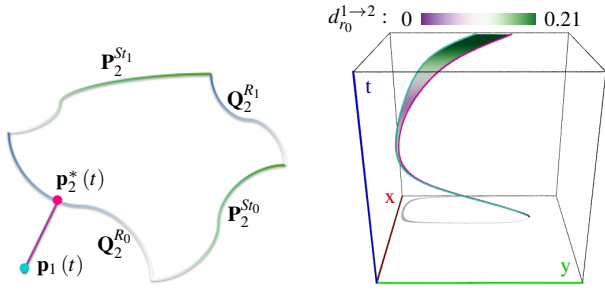
$$(R^*, St^*)(t) = \arg \min_{\substack{R \in [R_0, R_1] \\ St \in [St_0, St_1]}} \|\phi_{t_0}^{t-t_0}(\mathbf{x}_0, \mathbf{v}_0, r_0) - \psi_{t_0}^{t-t_0}(\mathbf{x}_0, \mathbf{v}_0, R, St)\| \quad (10)$$

We define the curve of closest match locations to a Model 1 trajectory $\mathbf{p}_1(t) = \phi_{t_0}^{t-t_0}(\mathbf{x}_0, \mathbf{v}_0, r_0)$ as $\mathbf{p}_2^*(t)$. Then, the closest match distance is equivalently given as $d_{r_0}^{1 \rightarrow 2}(t) = \|\mathbf{p}_1(t) - \mathbf{p}_2^*(t)\|$. Note that $\mathbf{p}_2^*(t)$ is not necessarily a continuous curve. We address this issue later in this section.

To visualize the closest matches, we display both the Model 1 trajectory $\mathbf{p}_1(t)$ in cyan and the closest match curve $\mathbf{p}_2^*(t)$ in magenta in space-time and triangulate the space between them, see Fig. 3 for an example. We additionally provide the possibility to color-code on the connecting surface either the closest match distance $d_{r_0}^{1 \rightarrow 2}$, or one of the closest match parameters R^* or St^* .

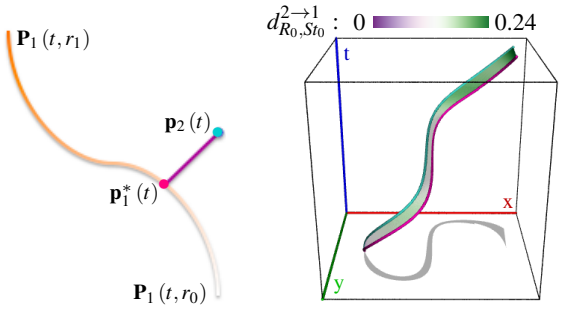
Closest Match from Model 2 to Model 1. Similarly, we define the closest match of a given Model 2 trajectory, seeded at (\mathbf{x}_0, t_0) , with initial velocity \mathbf{v}_0 , density ratio R_0 and Stokes number St_0 as:

$$d_{R_0, St_0}^{2 \rightarrow 1}(t) = \min_{r \in [r_0, r_1]} \|\psi_{t_0}^{t-t_0}(\mathbf{x}_0, \mathbf{v}_0, R_0, St_0) - \phi_{t_0}^{t-t_0}(\mathbf{x}_0, \mathbf{v}_0, r)\| \quad (11)$$



(a) Illustration of closest match from Model 1 to Model 2 volume. (b) Space-time visualization of closest matches over time.

Figure 3: In (a), the closest match from Model 1 to Model 2 is shown for time t . In (b), the closest matches are shown over time for seed $(x_0, y_0, t_0) = (1.4, 0.8, 0)$, and $\tau = 9,95$ in the DOUBLE GYRE. The cyan line is the Model 1 trajectory $\mathbf{p}_1(t)$ and the magenta line are the closest match locations $\mathbf{p}_2^*(t)$. Here, for $r_0 = 0.0491$ and Model 2 parameters $R \in [0.5, 0.7]$ and $St \in [0.0196, 0.4911]$.



(a) Illustration of closest match from Model 2 to Model 1 front line. (b) Space-time visualization of closest matches over time.

Figure 4: In (a), the closest match from Model 2 to Model 1 is shown for time t . In (b), it is shown for seed $(x_0, y_0, t_0) = (0.3, 0.5, 0)$ and duration $\tau = 9,95$ in the DOUBLE GYRE. The cyan line shows the Model 2 trajectory $\mathbf{p}_2(t)$ and the magenta line the closest match locations $\mathbf{p}_1^*(t)$. Here, for density ratio $R_0 = 0.5$, Stokes number $St_0 = 0.4911$ and response time $r \in [0.0020, 0.0491]$.

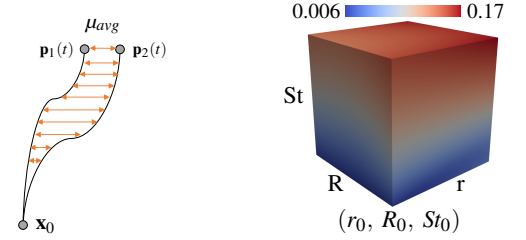
with response time r^* of Model 1, leading to the closest match:

$$r^*(t) = \arg \min_{r \in [r_0, r_1]} \|\Psi_{t_0}^{t-t_0}(\mathbf{x}_0, \mathbf{v}_0, R_0, St_0) - \Phi_{t_0}^{t-t_0}(\mathbf{x}_0, \mathbf{v}_0, r)\| \quad (12)$$

Same as above, we define the curve of closest matching locations as $\mathbf{p}_1^*(t)$. We visualize the closest matches by displaying the Model 2 trajectory $\mathbf{p}_2(t)$ in cyan and the closest matches in Model 1 $\mathbf{p}_1^*(t)$ in magenta, and triangulate the space between them. The resulting surface is color-coded by distance $d_{R_0, St_0}^{2 \to 1}$ or by the closest match inertial parameter r^* , see Fig. 4.

3.3. Parameter Space Visualization

In the third view, we provide a more quantitative approach. In total, both methods have three inertial parameters (r, R, St) that are viewed in a certain range, which can be seen as a 3D parameter space. Every point in this space uniquely defines the parameters of a trajectory



(a) Illustration of the distance measure

(b) Parameter space

Figure 5: Left: illustration of the trajectory distance measure. Right: parameter space visualization for the parameter ranges $r \in [0.0020, 0.0491]$, $R \in [0.5, 0.7]$ and $St \in [0.0196, 0.4911]$. For seed $(x_0, y_0, t_0) = (0.9, 0.6, 0)$ and integration duration $\tau = 9.95$.

for both models. In order to compare these two trajectories, we require a trajectory distance measure. In principle, numerous distance measures between two curves are imaginable. In the following, we assume that particles are seeded at point (\mathbf{x}_0, t_0) , with initial velocity \mathbf{v}_0 and response time r , density ratio R and Stokes number St . Further, we trace the particle over integration duration τ . We compare the trajectories $\mathbf{p}_1(t) = \Phi_{t_0}^t(\mathbf{x}_0, \mathbf{v}_0, r)$ and $\mathbf{p}_2(t) = \Psi_{t_0}^t(\mathbf{x}_0, \mathbf{v}_0, R, St)$ by the time-averaged Euclidean distance:

$$\mu_{avg}(r, R, St) = \frac{1}{\tau} \int_0^\tau \|\Phi_{t_0}^t(\mathbf{x}_0, \mathbf{v}_0, r) - \Psi_{t_0}^t(\mathbf{x}_0, \mathbf{v}_0, R, St)\| dt \quad (13)$$

The distance measure is illustrated in Fig. 5a. We not use the Hausdorff distance, as it computes distances among particles across different time steps. For visualization, we discretize the (r, R, St) space at one seed point and color-code the distances, as shown in Fig. 5b for the DOUBLE GYRE flow. To visualize the parameter space at multiple seed points, we later use multi-dimensional stacking.

4. Implementation

Since inertial particle motion is governed by a first-order ODE, we compute trajectories with a fourth-order Runge-Kutta integrator. Tracing integral surfaces in the space-time view requires adaptive refinement of the front line for long integration durations. In case of Model 1 the front line forms a sequence of line segments and in case of Model 2, the front line forms a closed polygon. The closest matches, cf. Eqs. (9)–(12), are computed by discretizing the other model's parameter intervals $[r_0, r_1]$, or $[R_0, R_1]$ and $[St_0, St_1]$, respectively. Thus, front lines consist of multiple discrete line segments. The closest point is either a vertex or a point on the segments.

5. Results

We apply our methods to multiple analytic and numerical data sets. For all experiments, we use a viscosity of air $\mu = 1.81 \times 10^{-5} \text{ kg/(m s)}$ and assume a gravity-free environment, i.e., $\mathbf{g} = \mathbf{0} \text{ m/s}^2$. All particles are released from rest with initial velocity $\mathbf{v}_0 = \mathbf{0} \text{ m/s}$ and have the density of sand $\rho_p = 1600 \text{ kg/m}^3$.

5.1. Influence of Particle Size

First, we study the influence of the particle size on the trajectory distances. For this, we introduce the DOUBLE GYRE vector field.

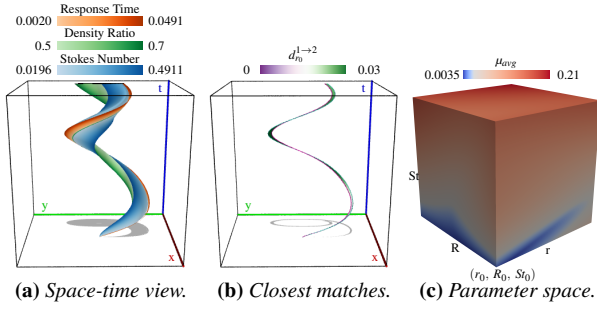


Figure 6: Results in the DOUBLE GYRE. Fig. 6a shows the space-time view, Fig. 6b the closest match distance $d_{r_0}^{1 \rightarrow 2}$ and Fig. 6c the parameter space for a particle seeded at $(x_0, y_0, t_0) = (1, 0.5, 0)$ with duration $\tau = 9.95$ and μ_{avg} as trajectory distance measure.

Double Gyre. The DOUBLE GYRE flow [SLM05] is an analytic and periodic 2D unsteady vector field. We define it on the domain $[0, 2] \times [0, 1] \times [0, 10]$ and use the parametrization:

$$\mathbf{u}(x, y, t) = \begin{pmatrix} -0.1\pi \sin(f(x, t)\pi) \cos(y\pi) \\ 0.1\pi \cos(f(x, t)\pi) \sin(y\pi) \frac{d}{dx}f(x, t) \end{pmatrix} \quad (14)$$

where

$$f(x, t) = 0.25 \sin\left(t \cdot \frac{\pi}{5}\right) x^2 + \left(1 - 0.5 \sin\left(t \cdot \frac{\pi}{5}\right)\right) x \quad (15)$$

Fig. 6 shows the space-time visualization, closest match distance from Model 1 to Model 2 and the parameter space visualization, with parameters $r \in [0.0020, 0.0491]$, $R \in [0.5, 0.7]$, $St \in [0.0196, 0.4911]$ and for an integration duration of $\tau = 9.95$. We observe that small particles behave similar in both models, which is apparent in space-time in Fig. 7, where the bright colored trajectories of small parameters match closely. This is because the response time and the Stokes number are proportional and since Model 1 assumes the fluid density to be much smaller than the particle density, cf. Section 2.1. Therefore, we expect Model 1 pathlines and Model 2 pathlines to be similar for low response times and low density ratios and Stokes numbers, respectively. This is especially apparent in the parameter space visualization in Fig. 6c. This visualization shows that differences increase quickly when the Stokes number increases, but there is a wide range of response times (and density ratios), in which trajectories are similar. From this visualization, we can read acceptable parameter ranges, in which we can select either particle model and obtain similar results for a certain parameter set.

In order to get a better impression of the time-dependent differences, we visualize the closest match distance $d_{r_0}^{1 \rightarrow 2}$ in Fig. 8 over time. It is apparent that with smaller response time r_0 the distance to the closest matching trajectory point of Model 2 gets smaller throughout the entire time range, up to the point where differences are visually indistinguishable. This visualization provides a comforting visual confirmation of the small differences for a particular parameter configuration, which is exhibiting less clutter than the direct space-time plot of the hull surfaces.

5.2. Influence of Seed Point

The shape of the created space-time surfaces strongly depends on the seed point. To demonstrate this, we use an analytic vector field.

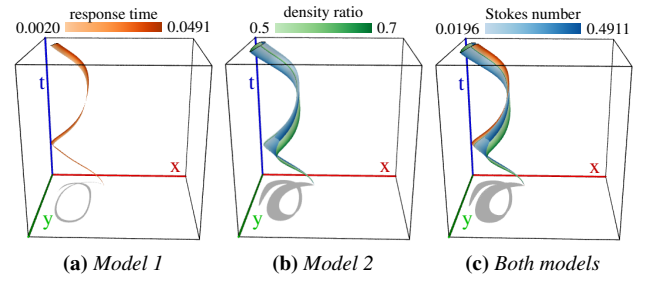


Figure 7: Space-time view of possible inertial particle trajectories for both models in the DOUBLE GYRE. Here, with seed point $(x_0, y_0, t_0) = (0.8, 0.2, 0)$, integration duration $\tau = 9.95$, $r \in [0.002, 0.0491]$, $R \in [0.5, 0.7]$ and $St \in [0.0196, 0.4911]$.

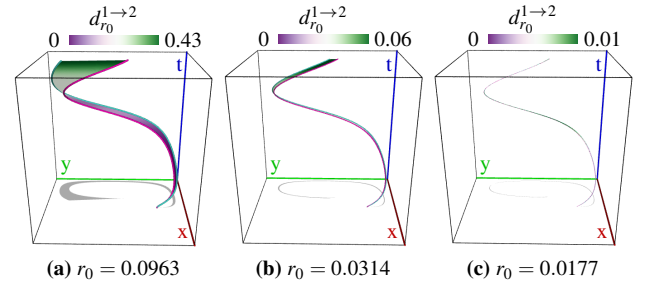


Figure 8: Closest matches for different response times in the DOUBLE GYRE. Here, with seed point $(x_0, y_0, t_0) = (1, 0.2, 0)$, integration duration $\tau = 9.95$, $R \in [0.5, 0.7]$ and $St \in [0.0196, 0.9626]$. With smaller response time r_0 the closest match distance $d_{r_0}^{1 \rightarrow 2}$ decreases.

Forced Damped Duffing. The FORCED DAMPED DUFFING oscillator [HS11] is an analytic 2D unsteady vector field. In Fig. 9, we observe it in the domain $[-2.5, 2.5] \times [-2.5, 2.5] \times [0, 12]$ and use the parametrization:

$$\mathbf{u}(x, y, t) = \begin{pmatrix} y \\ x - x^3 - 0.25y + 0.4 \cos t \end{pmatrix} \quad (16)$$

For the given seed point, the space-time visualization shows a significant stretching of the hull surface along the front representing the varying Stokes number. Similarly, the parameter space shows a very quickly increasing trajectory distance, when increasing the Stokes number. On the other hand, a change in the response time or the density ratio have a significantly smaller impact. A first conclusion is that the two models are interchangeable for small Stokes numbers, but how much does this conclusion depend on the seed point?

Fig. 10 shows the significantly different results for two different seeds in the FORCED DAMPED DUFFING flow. While a simultaneous visualization of multiple surfaces is possible, it quickly becomes infeasible due to occlusion problems. For this reason, we visualize the seed point dependence by displaying multiple stacked parameter spaces at different seed points in Fig. 11. We can see that trajectories are only similar inside the two vortices. In the outer part of the domain, particles accelerate in this analytic flow, amplifying particles differences quickly. We can see that the choice of an adequate particle model does not only depend on the considered parameter ranges, but also strongly depends on the seed point.

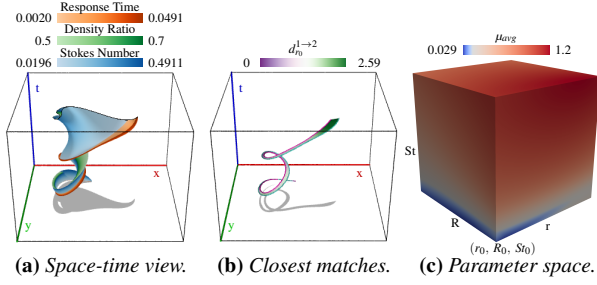


Figure 9: Results in the FORCED DAMPED DUFFING oscillator. Fig. 9a shows the space-time visualization, Fig. 9b the closest match distance $d_{r_0}^{1 \rightarrow 2}$ for response time $r_0 = 0.0491$ and Fig. 9c the parameter space for a particle seeded at $(x_0, y_0, t_0) = (-0.3, -1.2, 0)$ with duration $\tau = 10.1$ and trajectory distance μ_{avg} .

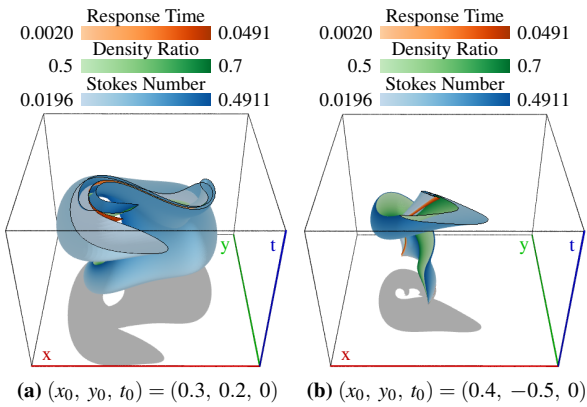


Figure 10: Space-time visualization for two different seed points in the FORCED DAMPED DUFFING oscillator. Here, for $\tau = 10.1$.

5.3. Examples in Numerical Flows

Square Cylinder. The SQUARE CYLINDER flow is a 3D numerical vector field, describing the flow around an obstacle. Tino Weinkauf provided a uniformly resampled version, based on the Navier-Stokes simulation by Camarri et al. [CSBIO5]. Its uniformity along one dimension allows us to treat one slice as a 2D unsteady vector field. The domain of the SQUARE CYLINDER vector field covers the ranges $x \in [0, 32]$, $y \in [0, 8]$, $t \in [0, 162]$. A space-time visualization, the closest match visualization and the parameter space are presented in Fig. 12, where the obstacle is colored purple. Vortices in the wake of the obstacle cause deviations between the models for larger particles. Thus, if wake turbulence is concerned, Model 1 cannot replace Model 2. In the laminar areas, however, particle trajectories are more similar. Further visible in the parameter space for a seed in front of the obstacle, Model 1 is a good fit for all considered density ratios and response times, as long as the Stokes number remains small. To get a more complete picture of the behavior for different seed points, Fig. 13 shows the stacked parameter space. A small Stokes number leads to small differences in the entire domain.

Boussinesq. The BOUSSINESQ flow is a 2D numerical unsteady convection simulation around a heated cylinder and was kindly provided by Tino Weinkauf. The domain covers the ranges $x \in$

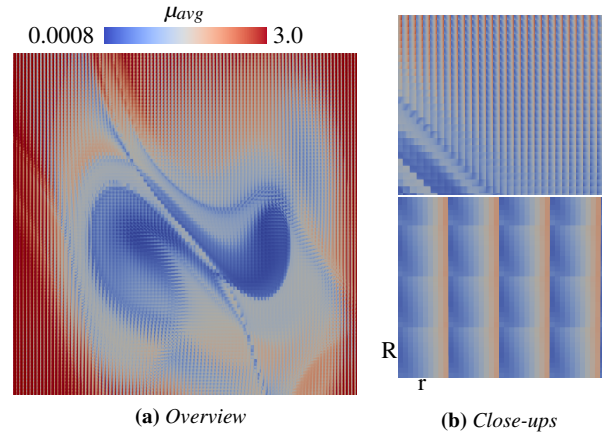


Figure 11: Stacked parameter spaces showing μ_{avg} for 100×100 seed points in the FORCED DAMPED DUFFING, with fixed Stokes number $St = 0.4911$, $\tau = 10.1$ and $[r_0, r_1] = [0.0020, 0.0491]$, $[R_0, R_1] = [0.3, 0.7]$. The parameter ranges are discretized to 10×10 . Fig. 11a gives an overview. When zooming in as in Fig. 11b, the parameter spaces of individual seed points become apparent.

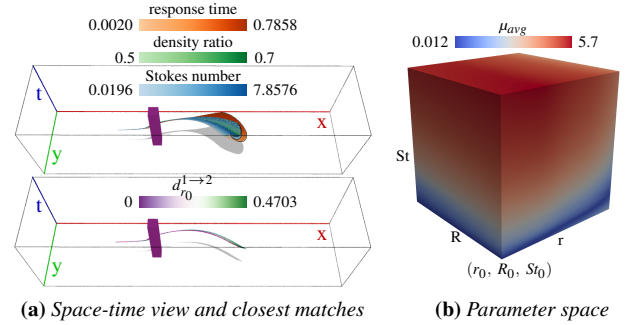


Figure 12: Results in the SQUARE CYLINDER flow. Left: space-time visualization and closest matches. Right: parameter space for a particle seeded at $(x_0, y_0, t_0) = (7.664, 3.771, 0)$ with $\tau = 15$.

Vector Field	Extraction Time
DOUBLE GYRE	22 min
FORCED DAMPED DUFFING	10 min
SQUARE CYLINDER	3 h 44 min
BOUSSINESQ	10 h 5 min

Table 1: Extraction time of the full parameter space in one seed point for trajectory measure μ_{avg} and duration $\tau = 10$.

$[-0.5, 0.5]$, $y \in [-0.5, 2.5]$, $t \in [0, 20]$. This flow serves as a test case for a more turbulent scenario. The differences in the slowly developing turbulent wake are larger. The stacked parameter space can be seen in Fig. 14, where we show slices of different Stokes numbers. In contrast to the previous example, differences are high for every particle size. With our visualizations, we can identify areas in which the simpler Model 1 trajectories cannot replace Model 2.

5.4. Performance

All experiments were conducted on an Intel Core i5-6300U CPU with 2.4 GHz and 8 GB RAM. The trajectory differences for the entire parameter space are precomputed. The precomputation timings

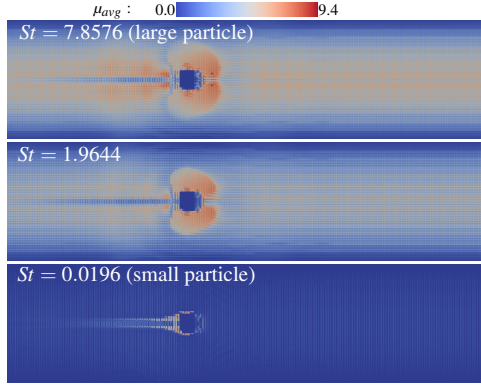


Figure 13: Stacked parameter spaces in the SQUARE CYLINDER for a 200×50 seed point grid with fixed Stokes number. The parameter ranges are discretized to 5×5 , for $r \in [0.0020, 0.7858]$, $R \in [0.3, 0.7]$, $St \in [0.0196, 7.8576]$, $t_0 = 0$ and $\tau = 15$.

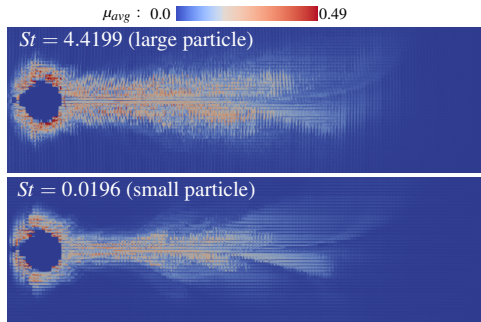


Figure 14: Stacked parameter spaces showing μ_{avg} for a 150×50 grid of seeds in the BOUSSINESQ flow with fixed Stokes number. The parameter ranges are discretized to a 5×5 grid. Here, with $[r_0, r_1] = [0.0020, 0.4420]$, $[R_0, R_1] = [0.3, 0.7]$, $t_0 = 0$ and $\tau = 6$.

are listed in Table 1, for a discrete grid of $100 \times 100 \times 100$ voxels in the parameter ranges of r, R and St . For the stacked parameter space visualization, we used a spatial resolution of 100×100 seed points and a smaller parameter space resolution of $10 \times 10 \times 10$.

5.5. Discussion

Occlusion. Depending on the data set, the space-time visualizations can exhibit a significant amount of occlusion. Fig. 15 illustrates this for a seed point $(x_0, y_0, t_0) = (-1.5, 1, 0)$ in the FORCED DAMPED DUFFING. In order to look inside, we use axis-aligned clipping planes to slice through the domain. An adjustment of the transparency is imaginable, as well [BWF*10, GTG17].

Initial velocity. Throughout all examples, we did not vary the initial velocity \mathbf{v}_0 , which would create another dimension. For a single particle model, the influence of the initial velocity has been studied for particle trajectories by Baeza Rojo et al. [BRGG18] and for Lagrangian coherent structures by Sagristà et al. [SJJ*17].

Two-way coupling. In this paper, we used inertial particle models that assume one-way coupling. In the future, we plan to apply our methods to the comparison of one-way coupled and two-way coupled trajectories. Note that two-way coupled trajectories are sig-

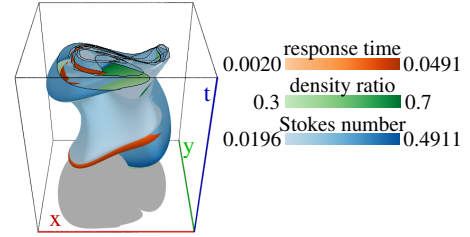


Figure 15: With long integration duration, surfaces tend to become complex and occlude themselves. Seed: $(x_0, y_0, t_0) = (-1.5, 1, 0)$, with integration duration $\tau = 10.1$ in FORCED DAMPED DUFFING.

nificantly more complicated to compute, thus an approximation by a parametric model might be very beneficial.

Hull Surfaces. The hull surfaces used to visualize the realization space of inertial trajectories in Model 2 is an approximation. Since inertial particle trajectories can intersect, inner trajectories might leave the volume in rare cases. A full Monte Carlo sampling of the entire volume is costly and we leave its investigation to future work.

Extraction time. We calculated the closest matches and the parameter space visualizations on the CPU. As shown in Section 5.4 this leads to a long precomputation time. To improve performance and interactivity, an implementation on the GPU is imaginable.

6. Conclusions

In this paper, we used multiple visualizations to compare two frequently used inertial particle models. First, we provided a qualitative view on the possible trajectories that inertial particles might take in space-time for various model parameters. In case of the first model, which has one inertial parameter, this results in a surface. For the second model, which has two inertial parameters, we obtain a volume, which we visualize by the four enclosing hull surfaces. Given a particle with some fix inertial parameters, we introduced the closest match, which describes the parameters and distance to the closest position that we could reach by switching the particle model. The closest match allowed us to express and visualize how similar the two models are for a given seed point. By expanding the visualization onto multiple seed points we inspected this similarity between models across the whole space-time domain. Finally, we introduced a metric to compare Model 1 and Model 2 trajectories quantitatively and visualized this measure in parameter space for one or multiple seed points using stacked visualization. With our method it is possible to locate parameter ranges and areas in the domain, in which two particle models are similar and interchangeable.

To generalize our method we will also have to take into account initial velocity and possibly other inertial parameters in future work. This means first of all that space-time visualizations will have to cover more than two varying inertial parameters, which would yield a more than three-dimensional space. Similarly, parameter spaces would also contain more than three dimensions if we varied the initial velocity. Even in higher dimensions, our method is still applicable to a three-dimensional subspace of the parameter space to visualize trajectory distances. Approximating a trajectory in another model and visualizing the resulting curves and their approximation error also works in a higher dimensional parameter space, but becomes computationally more expensive, as each potential parameter

combination could be the closest match. We also want to extend our method to three-dimensional data sets, which would result in a 4D space-time domain. While our quantitative method, i.e., the distance computation in the parameter space would still work in higher dimensional space-time, the actual visualization in space-time needs to handle the additional occlusion and high dimensionality. For this, new projections can be used, such as by Hofmann et al. [HRS18].

References

- [BBC*09] BENZI R., BIFERALE L., CALZAVARINI E., LOHSE D., TOSCHI F.: Velocity-gradient statistics along particle trajectories in turbulent flows: The refined similarity hypothesis in the Lagrangian frame. *Phys. Rev. E* 80 (Dec 2009), 066318. 2
- [BBC*11] BEC J., BIFERALE L., CENCINI M., LANOTTE A. S., TOSCHI F.: Spatial and velocity statistics of inertial particles in turbulent flows. *Journal of Physics: Conference Series* 333, 1 (2011), 012003. 2
- [BCPP00] BABIANO A., CARTWRIGHT J. H. E., PIRO O., PROVENZALE A.: Dynamics of a small neutrally buoyant sphere in a fluid and targeting in Hamiltonian systems. *Phys. Rev. Lett.* 84 (Jun 2000), 5764–5767. 2
- [BRGG18] BAEZA ROJO I., GROSS M., GÜNTHER T.: Visualizing the phase space of heterogeneous inertial particles in 2D flows. *Computer Graphics Forum (Proc. EuroVis)* 37, 3 (2018). 2, 7
- [BTT02] BENCIK I. J., TOROCZKAI Z., TÉL T.: Selective sensitivity of open chaotic flows on inertial tracer advection: Catching particles with a stick. *Phys. Rev. Lett.* 89 (Sep 2002), 164501. 2
- [BWF*10] BORN S., WIEBEL A., FRIEDRICH J., SCHEUERMANN G., BARTZ D.: Illustrative stream surfaces. *IEEE TVCG* 16, 6 (2010), 1329–1338. 7
- [CGP*10] CASCIOLA C. M., GUALTIERI P., PICANO F., SARDINA G., TROIANI G.: Dynamics of inertial particles in free jets. *Physica Scripta* 2010, T142 (2010), 014001. 2
- [CSBI05] CAMARRI S., SALVETTI M.-V., BUFFONI M., IOLLO A.: Simulation of the three-dimensional flow around a square cylinder between parallel walls at moderate reynolds numbers. *XVII Congresso di Meccanica Teorica ed Applicata* (11-15 September 2005). 6
- [CST98] CROWE C., SOMMERFIELD M., TSUJI Y.: Multiphase flows with droplets and particles. *CRC Press* (1998). 2
- [FBW16] FERSTL F., BÜRGER K., WESTERMANN R.: Streamline variability plots for characterizing the uncertainty in vector field ensembles. *IEEE TVCG* 22, 1 (2016), 767–776. 2
- [FH15] FARAZMAND M., HALLER G.: The Maxey–Riley equation: Existence, uniqueness and regularity of solutions. *Nonlinear Analysis: Real World Applications* 22 (2015), 98–106. 2
- [GG17] GÜNTHER T., GROSS M.: Flow-induced inertial steady vector field topology. *Computer Graphics Forum (Proc. Eurographics)* 36, 2 (2017), 143–152. 2
- [GKKT13] GÜNTHER T., KUHN A., KUTZ B., THEISEL H.: Mass-dependent integral curves in unsteady vector fields. *Proc. Eurovis* 32, 3 (2013), 211–220. 2, 3
- [GPPMn15] GARABOA-PAZ D., PÉREZ-MUÑUZURI V.: A method to calculate finite-time Lyapunov exponents for inertial particles in incompressible flows. *Nonlinear Proc. Geophys.* 22, 5 (2015), 571–577. 2
- [GT14] GÜNTHER T., THEISEL H.: Vortex cores of inertial particles. *IEEE Transactions on Visualization and Computer Graphics (Proc. IEEE SciVis)* 20, 12 (2014), 2535–2544. 2
- [GT15] GÜNTHER T., THEISEL H.: Finite-time mass separation for comparative visualizations of inertial particles. *Computer Graphics Forum (Proc. EuroVis)* 34, 3 (2015), 471–480. 2, 3
- [GT17] GÜNTHER T., THEISEL H.: Backward finite-time Lyapunov exponents in inertial flows. *IEEE Transactions on Visualization and Computer Graphics (Proc. IEEE SciVis 2016)* 23, 1 (2017), 970–979. 1, 2
- [GTG17] GÜNTHER T., THEISEL H., GROSS M.: Decoupled opacity optimization for points, lines and surfaces. *Computer Graphics Forum (Proc. Eurographics)* 36, 2 (2017), 153–162. 7
- [HOGJ13] HUMMEL M., OBERMAIER H., GARTH C., JOY K. I.: Comparative visual analysis of lagrangian transport in CFD ensembles. *IEEE TVCG* 19, 12 (Dec 2013), 2743–2752. 2
- [HRS18] HOFMANN L., RIECK B., SADLO F.: Visualization of 4D vector field topology. *Computer Graphics Forum (Proc. EuroVis)* 37, 3 (2018), 301–313. 8
- [HS08] HALLER G., SAPSIS T.: Where do inertial particles go in fluid flows? *Physica D: Nonlinear Phenomena* 237 (May 2008), 573–583. 2
- [HS11] HALLER G., SAPSIS T.: Lagrangian coherent structures and the smallest finite-time lyapunov exponent. *Chaos* 21, 2 (2011), 023115. 5
- [KGRK14] KUTZ B. M., GÜNTHER T., RUMPF A., KUHN A.: Numerical examination of a model rotor in brownout conditions. *Proceedings of the American Helicopter Society number AHS2014–000343* (2014). 1, 2
- [MLP*10] MCLOUGHLIN T., LARAMEE R. S., PEIKERT R., POST F. H., CHEN M.: Over two decades of integration-based, geometric flow visualization. *Computer Graphics Forum* 29, 6 (2010), 17–26. 1, 2
- [MR83] MAXEY M. R., RILEY J. J.: Equation of motion for a small rigid sphere in a nonuniform flow. *Physics of Fluids* 26, 4 (1983), 883–889. 2
- [MWK14] MIRZARGAR M., WHITAKER R. T., KIRBY R. M.: Curve boxplot: Generalization of boxplot for ensembles of curves. *IEEE TVCG* 20, 12 (Dec 2014), 2654–2663. 2
- [NWE74] NATUSCH D. F. S., WALLACE J. R., EVANS C. A.: Toxic trace elements: Preferential concentration in respirable particles. *Science* 183, 4121 (1974), 202–204. 1
- [PD09] PENG J., DABIRI J. O.: Transport of inertial particles by Lagrangian coherent structures: Application to predator–prey interaction in jellyfish feeding. *Journal of Fluid Mechanics* 623 (3 2009), 75–84. 1, 2
- [RSBE01] ROETTGER S., SCHULZ M., BARTELHEIMER W., ERTL T.: Automotive soiling simulation based on massive particle tracing. In *Data Visualization 2001*, Eurographics. Springer Vienna, 2001, pp. 309–317. 2
- [SBR15] SUDHARSAN M., BRUNTON S. L., RILEY J. J.: Lagrangian coherent structures and inertial particle dynamics. *ArXiv e-prints* (2015). 1512.05733. 2
- [SGL10] SYAL M., GOVINDARAJAN B., LEISHMAN J. G.: Mesoscale sediment tracking methodology to analyze brownout cloud developments. In *Proceedings of the American Helicopter Society, 66th Annual Forum* (2010). 1, 2
- [SH09] SAPSIS T. P., HALLER G.: Inertial particle dynamics in a hurricane. *Journal of the Atmospheric Sciences* (2009). 1, 2
- [SJJ*17] SAGRISTÀ A., JORDAN S., JUST A., DIAS F., NONATO L. G., SADLO F.: Topological analysis of inertial dynamics. *IEEE TVCG* 23, 1 (2017), 950–959. 2, 7
- [SL99] SHAO Y., LI A.: Numerical modelling of saltation in the atmospheric surface layer. *Boundary-Layer Meteorology* 91 (1999), 199–255. 1
- [SLM05] SHADDEN S. C., LEKIEN F., MARSDEN J. E.: Definition and properties of lagrangian coherent structures from finite-time lyapunov exponents in two-dimensional aperiodic flows. *Physica D: Nonlinear Phenomena* 212, 3–4 (2005), 271–304. 5
- [SPH11] SAPSIS T., PENG J., HALLER G.: Instabilities on prey dynamics in jellyfish feeding. *Bull Math Biol.* 73, 8 (2011), 1841–1856. 2
- [SRCV98] SHAW R. A., READE W. C., COLLINS L. R., VERLINDE J.: Preferential concentration of cloud droplets by turbulence: Effects on the early evolution of cumulus cloud droplet spectra. *Journal of the Atmospheric Sciences* 55, 11 (1998), 1976–1998. 1
- [VdMG06] VILELA R. D., DE MOURA A. P. S., GREBOGI C.: Finite-size effects on open chaotic advection. *Phys. Rev. E* 73 (2006), 026302. 2